

## The reionization of He II and the temperature evolution of the intergalactic medium \*

Yun-Chuan Yu, Chang-Shuo Yan and You-Jun Lu

National Astronomical Observatories, Chinese Academy of Sciences, Beijing 100012, China;  
[yyc213@126.com](mailto:yyc213@126.com)

Received 2013 May 13; accepted 2013 November 2

**Abstract** A number of observations suggest that He II in the intergalactic medium (IGM) was fully ionized at  $z \sim 3$ , probably by quasi-stellar objects (QSOs). Here we construct a simple model of a QSO to study the reionization of He II and the corresponding thermal evolution of the IGM. We assume that QSOs are triggered by major mergers of dark matter halos, and the luminosity evolution of individual QSOs is described by an initial accretion stage with a constant Eddington ratio and then a power-law decay driven by long term disk evolution or fueling. Once a QSO is triggered, it immediately ionizes its surrounding area as an ionized bubble. The resulting changes in size and volume of the bubble are determined by the luminosity evolution of the central QSO. With the emergence of more and more bubbles, they eventually overlap each other and finally permeate the whole universe. During the He II reionization, the IGM temperature increases due to the photoheating by the ionization processes. Applying the bubble model and considering various heating and cooling mechanisms, we trace the thermal evolution of the IGM and obtain the average IGM temperature as a function of redshift, which is very consistent with observations. The increase in IGM temperature due to the reionization of He II may be determined more accurately in the future, which may put robust constraints on the QSO model and the physics of He II reionization.

**Key words:** cosmology: theory — intergalactic medium: QSO

### 1 INTRODUCTION

It is widely accepted that the intergalactic medium (IGM) experienced two dramatic changes since the cosmic dark ages. The two most abundant elements, hydrogen and helium, were transformed from a completely neutral state to a highly ionized state because of ionizing photons emitted from luminous sources like galaxies and quasi-stellar objects (QSOs). The reionization of H I and He I happened earlier compared with He II (Giroux & Shapiro 1996), since the ionization threshold of H I (or He I), i.e., 13.6 eV (or 24.6 eV), is lower than that of He II (54.4 eV). After the first stars and galaxies turned on (at redshift  $z \sim 30 - 15$ ), the ultraviolet (UV) photons radiated by them gradually ionized H I and He I in the IGM. The reionization of He II could only proceed when sources with sufficiently hard spectra, such as QSOs, became abundant.

---

\* Supported by the National Natural Science Foundation of China.

Constraints from both the Gunn-Peterson trough in the spectra of the highest redshift QSOs (e.g. Fan et al. 2006) and polarization data from the cosmic microwave background (e.g. Larson et al. 2011) suggest that the reionization of HI was completed at  $z \sim 6 - 10$ . The completion of the He II reionization, however, happened at a later time of  $z \sim 3$  according to spectra of the He II Ly $\alpha$  forest in extreme UV (e.g. Jakobsen et al. 1994; Zheng et al. 2004; Fechner et al. 2006). QSOs are considered to be the most likely candidates responsible for the reionization of He II (Madau et al. 1999; Sokasian et al. 2002; Furlanetto & Oh 2008), though bright QSOs are rare and unlikely to substantially contribute to the ionizing photon budget for either HI or He I at  $z > 5$  (Dijkstra et al. 2004; Bolton & Haehnelt 2007; Jiang et al. 2008). Measurements of the He II Ly $\alpha$  optical depth show that the optical depth rises rapidly at  $z \geq 3$  with an increasing amount of patchiness (Zheng et al. 2004; Fechner et al. 2006). The rapid rise in the optical depth and the degree of patchiness suggest a detection of the late stage of He II reionization, though data from observations are still not sufficient to give a robust constraint on the redshift where the He II reionization was complete.

One of the main impacts of hydrogen and helium reionization was on the thermal state of the IGM, which is particularly true for low density regions, where photoheating was the dominant heating process (Hui & Gnedin 1997; Becker et al. 2011). The cooling time of the IGM in low density regions was long, and thus the IGM can retain some memory of when and how it was last heated and correspondingly how the universe reionized (e.g. Zaroubi 2013). Recently, Becker et al. (2011) and Bolton et al. (2012) reported new measurements of the IGM temperature derived from the Ly $\alpha$  forest over the redshift  $z \sim 2 - 6$ , which clearly showed an increase in temperature of the IGM at  $z \sim 3$ . The detected rise in the IGM temperature is probably evidence of the He II reionization beginning at  $z \geq 4.4$  and ending at  $z \sim 3$ , as suggested by opacity measurements of the He II Ly $\alpha$  forest (Becker et al. 2011).

In this paper, we study the reionization of He II and IGM temperature evolution over redshift  $2 - 6$  by using a simple QSO model and try to explain the observations by Becker et al. (2011) and Bolton et al. (2012). The paper is organized as follows. In Section 2, we construct a simple QSO model by adopting the major merger hypothesis and a universal light curve to describe the accretion history and luminosity evolution of individual QSOs. The model parameters are calibrated by simultaneously fitting the optical and hard X-ray QSO/AGN luminosity functions. In Section 3, we first adopt the light curve of QSOs determined by the calibrated model parameters to study the evolution of individual He III ionization bubbles. By convolving the evolution of individual He III bubbles with the generation rate of QSOs, we investigate the He II reionization and the corresponding IGM temperature evolution in Section 4. We find that the observational results obtained by Becker et al. (2011) and Bolton et al. (2012) can be explained well by our model. Discussion and conclusions are given in Section 5 and Section 6, respectively.

Throughout this paper, we adopt  $\Omega_m = 0.26$ ,  $\Omega_\Lambda = 0.74$ ,  $\Omega_b h^2 = 0.024$ ,  $h = 0.72$  and  $\sigma_8 = 0.85$  (Dunkley et al. 2009). We assume that the IGM has a primordial composition with a helium mass fraction of  $Y = 0.24$ . If not otherwise stated, all distances are expressed as comoving quantities.

## 2 A SIMPLE QSO MODEL

The QSO luminosity function (LF) is determined by two physical quantities: (1) the triggering rate of QSOs; and (2) the light curve, which represents the accretion history of massive black holes (MBHs) and the luminosity evolution of individual QSOs. On one hand, the accretion history of an MBH is directly reflected by the evolution of the QSO bolometric luminosity, denoted as  $L_{\text{bol}}(z; M_{\bullet,f}, z_i)$ , if assuming a constant radiative efficiency  $\epsilon$ . On the other hand, the triggering rate of QSOs can be described by the number density of MBHs with an initial mass  $M_{\bullet,i}$  (or equivalently a final mass  $M_{\bullet,f}$  for a fixed light curve) that were triggered at  $z_i$ , here denoted as  $\dot{G}(M_{\bullet,f}; z_i)$ . The growth rate

of an MBH is given by

$$\dot{M}_{\bullet}(\tau; M_{\bullet,f}) = \dot{M}_{\bullet}(z; M_{\bullet,f}, z_i) = \frac{(1 - \epsilon)L_{\text{bol}}(z; M_{\bullet,f}, z_i)}{\epsilon c^2}, \quad (1)$$

where  $c$  is the speed of light, and  $\tau = \int_z^{z_i} \left| \frac{dt}{dz} \right| dz$ . Then the bolometric LF of QSOs is given by

$$\frac{d\Phi(L_{\text{bol}}, z)}{dL_{\text{bol}}} = \int_z^{\infty} \left| \frac{dt}{dz_i} \right| dz_i \int dM_{\bullet,f} \dot{G}(M_{\bullet,f}; z_i) \delta(L_{\text{bol}} - \mathcal{L}_{\text{bol}}(z; M_{\bullet,f}, z_i)). \quad (2)$$

## 2.1 The Triggering Rate of QSOs

We assume that a QSO can be triggered once two dark matter halos with comparable mass merge with each other. We adopt this major merger hypothesis as minor mergers may only affect the outskirts of halos and galaxies, and play an insignificant role in triggering nuclear activities. We assume that major mergers of halos are followed by major mergers of galaxies within them, and QSOs are triggered immediately after the mergers of halos, though there might be a time delay between galaxy mergers and halo mergers. Therefore, the generation rate of QSOs at a given redshift is determined by two factors: (1) the merger rate of dark matter halos, and (2) the relationship between a dark matter halo and its central MBH.

Fakhouri & Ma (2008) find that the halo merger rate can be described by a universal form which only depends on mass ratio  $x$ , resulting mass of the merged halos  $M_{\text{H}}$  and redshift  $z$ ,

$$R(M_{\text{H}}, x, z) = R_0 \left( \frac{M_{\text{H}}}{10^{12} M_{\odot}} \right)^{\alpha} x^{\beta} \exp \left[ \left( \frac{x}{\bar{x}} \right)^{\gamma} \right] (1+z)^{\eta}, \quad (3)$$

where  $(\alpha, \beta, \gamma, \eta, R_0, \bar{x}) = (0.133, -1.995, 0.263, 0.0993, 0.0104, 9.27 \times 10^{-3})$  (Fakhouri et al. 2010). Integrating over  $x$  for major mergers (i.e.,  $1/3 < x < 1$ ), the merger rate at any redshift  $z$  can be expressed as

$$R(M_{\text{H}}, z) = \int_{1/3}^1 R(M_{\text{H}}, x, z) dx = R'_0 \left( \frac{M_{\text{H}}}{10^{12} M_{\odot}} \right)^{\alpha} (1+z)^{\eta}, \quad (4)$$

where  $R'_0 = 0.373$ .

Observations suggest that the mass of the MBH is tightly correlated with the mass of its host dark matter halo and the properties of its host galaxy (Ferrarese 2002; Bandara et al. 2009; Gebhardt et al. 2000; Tremaine et al. 2002). Booth & Schaye (2010) have demonstrated by numerical simulations that the masses of MBHs are determined by the potential and masses of their host halos. For a halo with mass of  $M_{\text{H}}$ , if it follows the Navarro-Frenk-White density distributions as simulations have suggested, on average the logarithmic mass of the MBH in its center is

$$\langle \log M_{\bullet,f} \rangle \propto \log \left[ f(s, y)(1+z)M_{\text{H}}^{5/3} \right], \quad (5)$$

where  $s$  is the concentration of the dark matter halo,  $y = r_{\text{ej}}/r_{\text{vir}}$  is the physical scale where the MBH self-regulation takes place,  $r_{\text{vir}}$  is the virial radius and

$$f(s, y) = \frac{s}{[\ln(1+s) - s/(1+s)]^2} \times \left( 1 - \frac{1}{(1+sy)^2} - \frac{2 \ln(1+sy)}{1+sy} \right). \quad (6)$$

The halo concentration can be described by  $s = A(M_{\text{H}}/M_{\text{pivot}})^B(1+z)^C$ , where  $M_{\text{pivot}} = 2 \times 10^{12} h^{-1} M_{\odot}$ ,  $A = 5.71$ ,  $B = -0.084$  and  $C = -0.47$  (Duffy et al. 2008). Booth & Schaye (2010) find  $y = 0.22$  in order to match their simulation results with the observations.

Recent observations suggest that the stellar mass of the central galaxy in a cluster is proportional to its halo mass to the power of 1/3 (Brown & Brown 2010). To reflect this, we adopt a modified form for the relation between the mass of the MBH and the halo properties, i.e.,

$$\langle \log M_{\bullet,f} \rangle = \log \left[ \frac{\mathcal{B}(1+z)f(s,y)}{\left(\frac{M_H}{M_z^*}\right)^{-5/3} + \left(\frac{M_H}{M_z^*}\right)^{-1/3}} \right], \quad (7)$$

where  $M_z^* = M_0^*(1+z)^\alpha$ , and  $M_0^*$ ,  $\alpha$  and  $\mathcal{B}$  are free parameters that can be constrained by observations.

Equation (7) gives the mean logarithmic masses of MBHs in halos with mass  $M_H$ , but the real MBH logarithmic masses may scatter around this value. To reflect this, we assume that the distribution of the real logarithmic masses of MBHs around the mean value,  $P(\log M_{\bullet,f} | \langle \log M_{\bullet,f} \rangle)$ , is Gaussian with a standard deviation of 0.3 dex, similar to that of the  $M_\bullet - \sigma$  relation. Probably not every major merger of dark matter halos can lead to nuclear activity. We assume that only a fraction of major mergers can lead to the formation of a QSO, and this fraction depends on the mass of dark matter halos as

$$F(M_H) = \begin{cases} \left(\frac{M_H}{M_{\text{cut}}}\right)^{k_m}, & \text{if } M_H \leq M_{\text{cut}}, \\ 1, & \text{if } M_H \geq M_{\text{cut}}. \end{cases} \quad (8)$$

Then the generation rate of QSOs is given by

$$\dot{G}(M_{\bullet,f}; z_i) = \int_0^\infty \frac{P(\log M_{\bullet,f} | \langle \log M_{\bullet,f} \rangle) R(M_{H,i}; z_i)}{M_{\bullet,f} \ln(10) |dt/dz_i|} F(M_{H,i}) \frac{dn(M_{H,i}; z_i)}{dM_{H,i}} dM_{H,i}, \quad (9)$$

where the halo mass function  $dn(M_{H,i}; z_i)/dM_{H,i}$  is given by the fitting formula in Sheth & Tormen (1999). For the generation rate of QSOs, the model parameters involved are  $(M_0^*, \alpha, \mathcal{B}, k_m, M_{\text{cut}})$ .

## 2.2 The QSO Light Curve

We assign each QSO a universal light curve, which describes two phases of accretion (e.g. Small & Blandford 1992; Yu & Lu 2004, 2008): in the first phase, the central MBH accretes surrounding material via a rate proportional to the Eddington limit,  $\dot{M}_{\text{acc}} = \lambda_0 \dot{M}_{\text{Edd}}$ , where  $\lambda_0$  is the Eddington ratio, and the QSO radiates at a bolometric luminosity of  $L = \lambda_0 L_{\text{Edd}}$ , where  $L_{\text{Edd}} = 1.26 \times 10^{46} (M_\bullet/10^8 M_\odot) \text{ erg s}^{-1}$  and  $\dot{M}_{\text{Edd}} = L_{\text{Edd}}/\epsilon c^2$ .

While a fraction  $\epsilon$  of the infalling matter is radiated away, the remaining  $(1-\epsilon)$  feeds the central MBH, which is the growth rate of the MBH  $\dot{M}_\bullet = (1-\epsilon)\dot{M}_{\text{acc}}$ . Therefore, the evolution of the luminosity in the first phase is given by

$$L(\tau) = \lambda_0 L_{\text{Edd,P}} \exp\left(\frac{\tau - \tau_P}{\tau_S}\right), \quad \text{for } \tau < \tau_P, \quad (10)$$

where  $\lambda_0 L_{\text{Edd,P}}$  is the peak luminosity and  $\tau_S = 4.5 \times 10^8 \text{ yr } \lambda_0^{-1} \epsilon / (1-\epsilon)$  is the Salpeter timescale. The mass of the MBH in the first phase evolves as

$$M_\bullet^I = M_{\bullet,P} \exp\left(\frac{\tau - \tau_P}{\tau_S}\right), \quad \text{for } \tau < \tau_P, \quad (11)$$

where  $M_{\bullet,P}$  is the peak mass of the MBH, and  $L_{\text{Edd,P}}$  is the Eddington luminosity of an MBH with mass  $M_{\bullet,P}$ .

The luminosity of the MBH increases exponentially until it reaches its peak luminosity at time  $\tau_P = \xi \tau_S$  ( $\xi$  is a dimensionless parameter), and then due to the feedback, the evolution of luminosity changes and enters a declining phase. In this second phase, the accretion by the MBH gradually

becomes inefficient and eventually terminates. The evolution of luminosity in this phase follows a power-law, i.e.,

$$L(\tau) = \lambda_0 L_{\text{Edd,P}} \left( \frac{\tau + \tau_{\text{D}} - \tau_{\text{P}}}{\tau_{\text{D}}} \right)^{-\gamma}, \quad \text{for } \tau_{\text{P}} < \tau < \tau_{\text{P}} + \eta\tau_{\text{D}}, \quad (12)$$

where  $\tau_{\text{D}} = \zeta\tau_{\text{S}}$  ( $\zeta$  is a dimensionless parameter) is the characteristic decay timescale of the luminosity,  $\eta = 10^{3/\gamma} - 1$  is set by assuming that the nuclear activity terminates once its luminosity declines to less than  $10^{-3}$  of its peak luminosity, and the duration of the second phase is  $\eta\zeta\tau_{\text{S}}$ . The mass of the MBH in the second phase evolves as

$$M_{\bullet}^{\text{II}} = M_{\bullet,\text{P}} \left\{ 1 + \frac{\zeta}{\gamma - 1} \left[ 1 - \left( \frac{\tau + \tau_{\text{D}} - \tau_{\text{P}}}{\tau_{\text{D}}} \right)^{1-\gamma} \right] \right\}, \quad \text{for } \tau_{\text{P}} < \tau < \tau_{\text{P}} + \eta\tau_{\text{D}}. \quad (13)$$

For the QSO light curve, the model parameters involved are  $(\epsilon, \xi, \zeta, \gamma)$ . According to Yu & Tremaine (2002), hereafter we adopt  $\epsilon = 0.1$ .

### 2.3 The QSO Luminosity Function

The observationally determined QSO LFs are given in either the optical band or the X-ray band. To constrain the parameters involved in the above QSO model, it is necessary to derive the QSO LFs at the same band as that of the observations. Below we introduce the bolometric correction (BC) for a given band Y,  $C_{\text{Y}} = L_{\text{bol}}/\nu L_{\nu}|_{\nu=Y}$ , where  $\nu L_{\nu}|_{\nu=Y}$  is the monochromatic luminosity at the central frequency of the Y-band.

According to Hopkins et al. (2007), the estimated BC in a given band Y depends on luminosity and is defined by

$$\langle \log C_{\text{Y}} \rangle = \log \left[ c_1 \left( \frac{L_{\text{bol}}}{10^{10} L_{\odot}} \right)^{k_1} + c_2 \left( \frac{L_{\text{bol}}}{10^{10} L_{\odot}} \right)^{k_2} \right], \quad (14)$$

with  $(c_1, k_1, c_2, k_2) = (10.83, 0.28, 6.08, -0.020)$  in the hard X-ray and  $(c_1, k_1, c_2, k_2) = (6.25, -0.37, 9.00, -0.012)$  in the B-band. The effective dispersion in the BC in different bands as a function of bolometric luminosity is

$$\sigma_{\log(L_{\text{bol}}/L_{\text{B}})} = \sigma_1 (L_{\text{bol}}/10^9 L_{\odot})^{\beta} + \sigma_2, \quad (15)$$

with  $(\sigma_1, \beta, \sigma_2) = (0.06, 0.10, 0.08)$  in the hard X-ray band and  $(\sigma_1, \beta, \sigma_2) = (0.08, -0.25, 0.060)$  in the B-band. To take into account the correction for extinction in the different observed bands, we need to adopt an obscuration fraction as a function of luminosity, which can be parameterized as a power law,

$$F_{\text{Y}}(L_{\text{bol}}) = f_{46} \left( \frac{L_{\text{bol}}}{10^{46} \text{ erg}^{-1}} \right)^{\beta}. \quad (16)$$

This gives values  $(f_{46}, \beta) = (1.243, 0.066)$  for the hard X-ray band and  $(0.260, 0.082)$  for the B-band (Hopkins et al. 2007). The obscuration fraction should be added into the integration when estimating the optical QSO LF. Then the LF in any given Y-band can be obtained as

$$\begin{aligned} \frac{d\Phi(L_{\text{Y}}, z)}{dL_{\text{Y}}} &= \iiint_z^{\infty} G(M_{\bullet,f}; z_i) \delta \left( L_{\text{Y}} - \frac{\mathcal{L}_{\text{bol}}(z; M_{\bullet,f}, z_i)}{C_{\text{Y}}} \right) \\ &\times F_{\text{Y}}(L_{\text{Y}} C_{\text{Y}}) P(\log C_{\text{Y}} | \langle \log C_{\text{Y}} \rangle) \left| \frac{dt}{dz_i} \right| dz_i dM_{\bullet,f} d \log C_{\text{Y}}, \end{aligned} \quad (17)$$

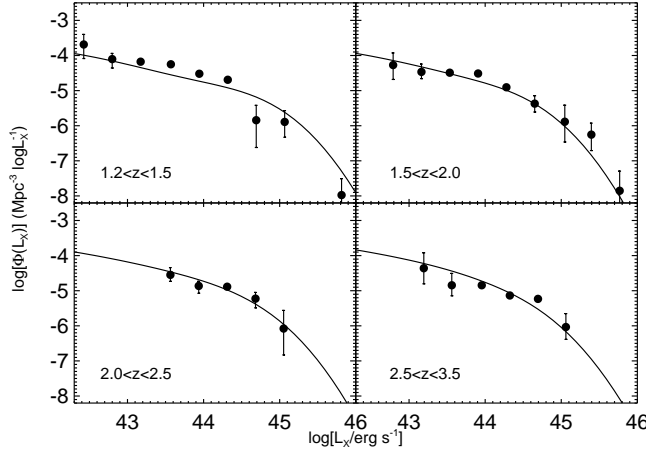


**Fig. 1** The QSO LFs in the hard X-ray band (2–10 keV). Circles represent the hard X-ray LFs obtained by Aird et al. (2010). The solid lines represent the QSO LFs obtained from the QSO model in this paper that best fit the observations.

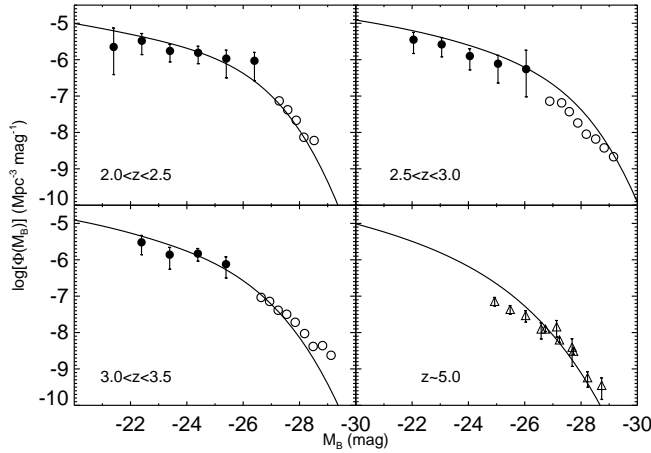


**Fig. 2** The QSO LFs in the B-band. The filled and open circles represent the observationally determined LFs by Bongiorno et al. (2007) and Richards et al. (2006), respectively. The triangles in the last figure represent that obtained by McGreer et al. (2013) at high redshift  $z \sim 5$ . The solid lines show the QSO LF obtained from the QSO model that best fits the observational data.

where  $P(\log C_Y | \langle \log C_Y \rangle)$  is assumed to be a Gaussian distribution of  $\log C_Y$  around the mean value  $\langle \log C_Y \rangle$  for any given  $L_{\text{bol}}$ .

Given the BCs and the obscuration fraction as above, the QSO LFs can be modeled in both the optical band and hard X-ray band for a given set of model parameters. Using the simple QSO model above, we use the Markov Chain Monte Carlo method to simultaneously fit the hard X-ray LFs and optical LFs. We obtain the best fits of the model parameters, i.e.,  $(M_0^*, \alpha, \mathcal{B}, k_m, M_{\text{cut}}) = (10^{13.9} M_\odot, -1.27, 10^{10.172} M_\odot, 0.539, 10^{14.45} M_\odot)$  and  $(\xi, \zeta, \gamma) = (2.019, 0.018, 1.045)$ . There could be some degeneracies among the model parameters. For example, if different forms for the

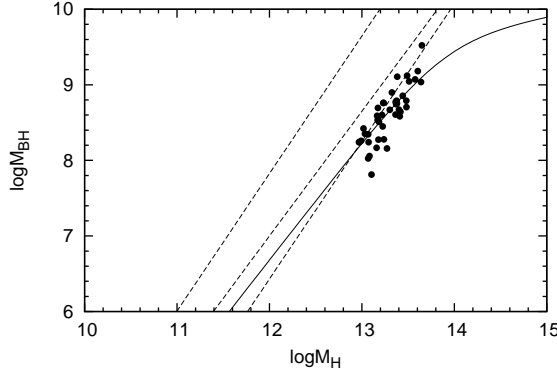


**Fig. 3** The  $M_{\bullet,f} - M_H$  relation. The solid curve represents the  $M_{\bullet,f} - M_H$  relation constrained by the QSO model in this paper at redshift  $z = 0$ . The circles are the objects from Bandara et al. (2009), in which the MBH masses are estimated by using the empirical relations and the halo masses are estimated by using the gravitational lensing technique. The three dashed lines, from left to right, represent the estimated  $M_{\bullet,f} - M_H$  relation at  $z = 0$  as described by eqs. (4), (6) and (7) in Ferrarese (2002), respectively.

$M_{\bullet,f} - M_H$  relation and/or the light curves are adopted, statistically good fits may also be obtained. Here we do not intend to go into details about the degeneracy of these model parameters, and the effects of choosing forms for the  $M_{\bullet,f} - M_H$  relation and/or the light curves different from those adopted by Equations (7), (10) and (12).

As seen from Figures 1 and 2, the observationally determined hard X-ray LFs and optical QSO LFs over redshift range (1.5–5) can be well fitted by our model. Figure 3 shows the  $M_{\bullet,f} - M_H$  relation at  $z = 0$  constrained by the QSO model that best fits the QSO LFs, which is clearly consistent with the observational results by Bandara et al. (2009) and Ferrarese (2002).

### 3 THE VOLUME EVOLUTION OF IONIZED BUBBLES

The evolution of an expanding He III bubble can be simply described by

$$\frac{dV}{dt} = \frac{\dot{N}_{\text{ion}}}{n_{\text{He II}}} - \frac{V}{t_{\text{rec}}}, \quad (18)$$

where the mean density  $n_{\text{He II}} = n_{\text{He II},0}(1+z)^3$ ,  $n_{\text{He II},0}$  is the mean density of helium at present,  $\dot{N}_{\text{ion}}$  is the emission rate of ionizing photons,  $V$  is the comoving volume of the He III bubble and  $t_{\text{rec}}$  is the recombination time of He III defined as  $t_{\text{rec}} = (C\alpha_A n_e)^{-1}$ , here  $C$  is a volume averaged clumping factor, given by  $C = \langle n_{\text{He II}}^2 \rangle / n_{\text{He II}}^2$ ,  $n_e = n_{\text{H}} + 2n_{\text{He}}$  and  $\alpha_A = 2.18 \times 10^{-12} \text{ cm}^3 \text{ s}^{-1}$  is the case A recombination coefficient of He III at  $T \sim 20\,000 \text{ K}$ . The recombination timescale can be expressed in terms of the Hubble time,  $t_{\text{H}} \approx 2/3H(z)^{-1}$ , as (McQuinn et al. 2009)

$$\frac{t_{\text{rec}}}{t_{\text{H}}} \approx \frac{0.6}{C} \left( \frac{T}{10^4 \text{K}} \right)^{0.7} \left( \frac{1+z}{4} \right)^{-3/2} \Delta_{\text{b}}^{-1}, \quad (19)$$

where  $\Delta_{\text{b}} = 1 + \delta_{\text{b}}$ , and  $\delta_{\text{b}}$  is the overdensity of gas.

Given the spectral energy distribution (SED) of a QSO, the injection rate of ionizing photons by the QSO can be easily obtained. Here we adopt an SED that follows a power law with a slope

of  $-1.57$  at  $\lambda \leq 1300 \text{ \AA}$  and  $-0.44$  at  $1 \mu\text{m} \geq \lambda \geq 1300 \text{ \AA}$  (Telfer et al. 2002). With the SED, the ionizing photon emission rate of the resulting QSO is

$$\dot{N}_{\text{ion}} = \frac{L_{\text{B}}}{\nu_{\text{B}}} \left( \frac{1300}{4400} \right)^{0.44} \int_{\nu_{\text{He III}}}^{\infty} \frac{1}{h\nu} \left( \frac{\nu}{\nu_{1300}} \right)^{-1.57} d\nu = 2.09 \times 10^{55} \text{ s}^{-1} \left( \frac{L_{\text{B}}}{10^{12} L_{\odot}} \right), \quad (20)$$

$\nu_{\text{He III}}$  is the frequency evaluated at the threshold for He II ionization ( $228 \text{ \AA}$ ) and  $\nu_{\text{B}}$  is the frequency corresponding to the center of the B-band,  $4400 \text{ \AA}$ .

Due to the obscuration, however, the ionized region is cone-like (with an opening angle) rather than spherical. In the unified model of QSOs/AGN, the observable properties of a particular QSO depend on the viewing angle relative to the central accretion disk. A type 2 QSO is presumably heavily obscured by a dense, dusty torus in the direction of the line of sight and its intrinsic continuum emission is highly absorbed by the torus, but a type 1 QSO is not obscured simply because the torus is not in the direction of the line of sight. So, the real volume of ionized material caused by a central QSO, either a type 1 or a type 2 case, is

$$V_{\text{real}} = \frac{\Omega}{4\pi} V_{\text{sph}}, \quad (21)$$

where  $\Omega$  is the solid angle opened by the ionized cone and  $V_{\text{sph}}$  is the volume of the spherical ionized region without considering the obscuration fraction. For a QSO with a given  $L_{\text{bol}}$ , we adopt  $\Omega/4\pi = F_{\text{B}}(L_{\text{bol}})$ , where  $F_{\text{B}}(L_{\text{bol}})$  is the ratio of type 1 QSOs to total QSOs as shown by Equation (16).

Figure 4 shows the radius evolution of a cone-like bubble. The bubble radius shown in this figure is the effective radius,

$$R_{\text{eff}}^3 = g_{\text{bubble}} R_{\text{max}}^3 = \int_0^{R_{\text{max}}} 3x_i(R) R^2 dR, \quad (22)$$

where  $g_{\text{bubble}}$  is the volume averaged ionization fraction in the bubble, and  $x_i(R)$  is the ionization fraction evolution at a given radius,  $R$ . Then the bubble volume can be expressed as  $V = (4\pi/3) R_{\text{eff}}^3$ . After the bubble reaches its maximum radius,  $R_{\text{max}}$ , the ionization fraction in the bubble declines due to the recombination of He II and the decrease in the injection rate of ionizing photons, but the volume of the bubble is still constant, until the outer region is completely recombined. Once the bubble reaches its maximum radius, the photon injection rate decreases due to the decline in the luminosity of the central QSO. Firstly, at a given time  $t_{\text{tp}}$  we need to determine the turning point,  $R_{\text{tp}}$ , the radius within which the recombination can still be balanced by the emission rate.

$$\dot{N}_{\text{ion}}(t_{\text{tp}}) = \frac{4\pi}{3} R_{\text{tp}}^3 C \alpha_{\text{A}} n_{\text{e}} n_{\text{He III}}. \quad (23)$$

Since there are no ionizing photons transmitted to the region out of the turning point, the ionization state evolution, at a given time  $t_i$  once the bubble reaches its maximum radius, is

$$x_i(R) = \int_{t_{\text{tp}}}^{t_i} -C \alpha x_i(R) n_{\text{e}} dt. \quad (24)$$

Figure 5 shows the evolution of the ionizing fraction after the bubble reaches its maximum radius, in a time interval of 25, 50, 100, 200 and 400 Myr from top to bottom. In our model, the central QSO continues shining at a lower luminosity to prevent the bubble from quickly recombining. In the inner regions, the ionization fraction drops at a slower rate, but in the outer regions it decrease faster due to the lack of ionizing photons. In the same figure, the dashed line shows the effective radius given by Equation (18) with the time interval of 25, 50, 100, 200 and 400 Myr once the bubble reaches its maximum radius from right to left.

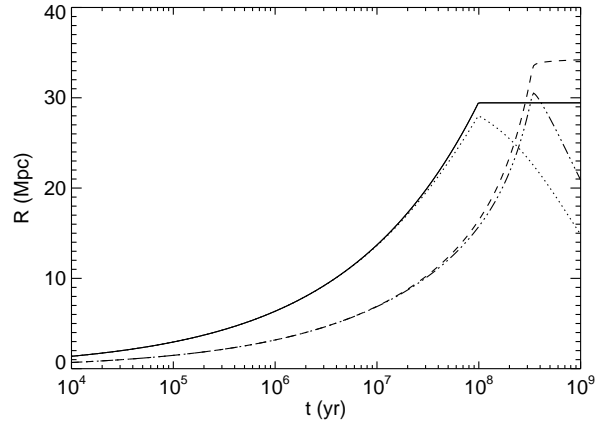


**Fig. 4** Effective radius evolution of an ionized bubble. The solid line and dotted line represent the radius evolution of an ionized cone-like bubble associated with a central QSO that radiates via a constant B-band luminosity of  $10^{12} L_{\odot}$  over a period of  $10^8$  yr at  $z = 3$  for clumping factors of  $C = 0$  and  $C = 3$ , respectively. The dashed line ( $C = 0$ ) and dot-dashed line ( $C = 3$ ) represent the radius evolution of an ionized cone-like bubble associated with a QSO that follows the light curve described by Eqs. (10) and (12), respectively, with a peak luminosity of  $10^{12} L_{\odot}$  at the B-band.

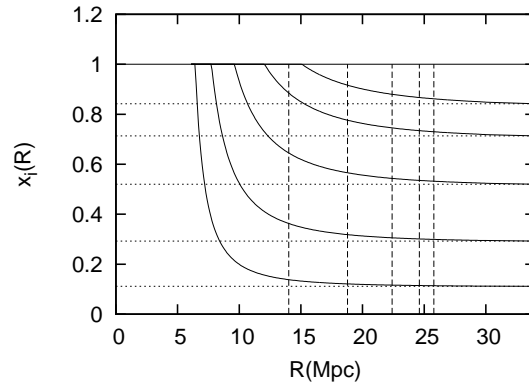


**Fig. 5** Ionizing fraction,  $x_i$ , at different radii within a bubble after it reaches the maximum size (for a QSO with a light curve given by Eqs. (10) and (12) with a peak luminosity of  $10^{12} L_{\odot}$  at the B-band). The solid lines show the ionizing fraction evolution in the time interval of 25, 50, 100, 200 and 400 Myr once the bubble reaches its maximum radius from top to bottom. The dashed lines show the effective radius given by Eq. (18) with the time interval of 25, 50, 100, 200 and 400 Myr once the bubble reaches its maximum radius from right to left respectively. The dotted lines are the corresponding ionizing fraction evolution in the case in which the central QSO shuts off once it reaches the maximum volume.

Figure 5 also shows the ionizing fraction evolution in the case that the central QSO shuts off once it reaches the maximum volume. In this case, the ionizing fraction at different radii drops simultaneously, since only recombination is present. Ignoring the later low luminosity stage of the central source obviously leads to underestimates of the ionization fraction in the bubble after it reaches its maximum volume.

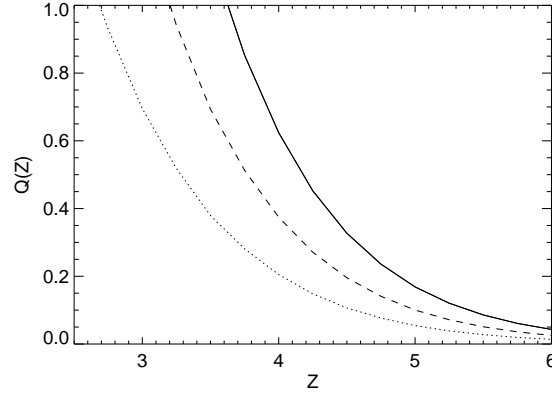


**Fig. 6** The He II reionization history. The solid, dashed and dotted lines represent the evolution of He II ionization with  $C = 0, 1$  and  $3$ , respectively.

Then the volume filling factor of He III,  $Q_{\text{He III}}(z)$ , can be determined by

$$Q_{\text{He III}}(z) = \int d \log C_B \int dL_{\text{bol}} \int dM_{\bullet, f} \int_z^\infty dz_i \int_{z_i}^z dz' \frac{dV_{\text{real}}}{dz'} \left( z'; \frac{L_{\text{bol}}}{C_B}, M_{\bullet, f}, z_i \right) \times \dot{G}(M_{\bullet, f}; z_i) \delta \left( L_B - \frac{\mathcal{L}_{\text{bol}}(z'; M_{\bullet, f}, z_i)}{C_B} \right) P(\log C_B | \langle \log C_B \rangle). \quad (25)$$

Figure 6 shows the He II ionization history, with values of a clumping factor given by  $C = 0$ ,  $C = 1$  and  $C = 3$ . The  $C = 3$  model shows that the He II reionization occurred at redshift  $z \sim 2.7$ , consistent with the observational results mentioned in Section 1 and other analytical models (e.g. Furlanetto & Oh 2008; Haardt & Madau 2012). The contribution of active bubbles,  $Q_{\text{active}}$ , can be calculated by

$$Q_{\text{active}}(z) = \int d \log C_B \int dL_{\text{bol}} \int dM_{\bullet, f} \int_\infty^z dz_i \int_{z_i}^z dz' \frac{dV_{\text{real}}}{dz'} \left( z'; \frac{L_{\text{bol}}}{C_B}, M_{\bullet, f}, z_i \right) \times \dot{G}(M_{\bullet, f}; z_i) \delta \left( L_B - \frac{\mathcal{L}_{\text{bol}}(z'; M_{\bullet, f}, z_i)}{C_B} \right) \times P(\log C_B | \langle \log C_B \rangle) \Theta_1(z_{\text{eq}} - z_i), \quad (26)$$

where  $z_{\text{eq}} = z_{\text{eq}}(z, z_i)$  is the redshift at which a QSO, triggered at  $z_{\text{eq}}$ , reaches its maximum volume at  $z$ , and the step function  $\Theta_1 = 1$  for  $z_i \leq z_{\text{eq}}$  or  $\Theta_1 = 0$  for  $z_i \geq z_{\text{eq}}$ . The corresponding equilibrium timescale,  $\tau_{\text{eq}}$ , can be set by integrating Equation (18) over time until the maximum volume is reached. The contribution of fossil bubbles,  $Q_{\text{fossil}}$ , can be calculated by

$$Q_{\text{fossil}}(z) = \int d \log C_B \int dL_{\text{bol}} \int dM_{\bullet, f} \int_\infty^z dz_i \int_{z_i}^z dz' \times \frac{dV_{\text{real}}}{dz'} \left( z'; \frac{L_{\text{bol}}}{C_B}, M_{\bullet, f}, z_i \right) \dot{G}(M_{\bullet, f}; z_i) \delta \left( L_B - \frac{\mathcal{L}_{\text{bol}}(z'; M_{\bullet, f}, z_i)}{C_B} \right) \times P(\log C_B | \langle \log C_B \rangle) \Theta_2(z_i - z_{\text{eq}}), \quad (27)$$

where the step function  $\Theta_2 = 1$  for  $z_i \geq z_{\text{eq}}$  or  $\Theta_2 = 0$  for  $z_i \leq z_{\text{eq}}$ , and  $z_{\text{eq}} = z_{\text{eq}}(z, z_i)$  is the redshift at which a QSO, triggered at  $z_{\text{eq}}$ , reaches its maximum volume at  $z$ .

Figure 7 shows the contribution to ionization due to different parts of the IGM (see Sect. 4. for details). It clearly shows that at the end of He II reionization, most bubbles are fossil bubbles.

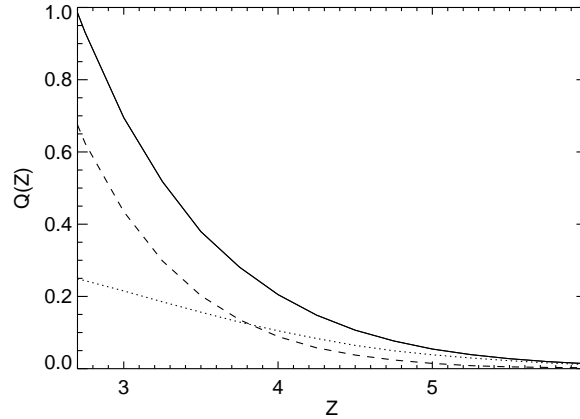


**Fig. 7** The contribution to ionization due to active bubbles and fossil bubbles. The solid line shows the He II reionization history by assuming a clumping factor of  $C = 3$ . The dashed line shows the contribution from the fossil bubbles, while the dotted line shows that from the active bubbles.

#### 4 THE IGM TEMPERATURE EVOLUTION DUE TO HE II REIONIZATION

The IGM has experienced two significant transitions, the reionization of hydrogen and helium. During the reionization, the excess energy released by photoionization passes to the electrons and thus increases the temperature of the IGM. In this paper, we focus on the impact of the helium reionization and corresponding temperature evolution of the IGM.

Generally, the temperature increase of the ionized gas after reionization is simply given by (Miralda-Escudé & Rees 1994)

$$k\Delta T = \frac{\langle E \rangle - E_0}{3}, \quad (28)$$

where  $\langle E \rangle$  is the average energy of the ionizing photons, and  $E_0$  is the energy needed per ionization in a mixture of hydrogen and helium gas. There are several thermal processes, such as photoionization heating, adiabatic cooling and recombination cooling, that can affect the IGM temperature. With these processes, the IGM temperature evolution is given by

$$\frac{dT}{dt} = -2HT + \frac{2T}{3(1+\delta)} \frac{d\delta}{dt} - \frac{T}{\Sigma_i X_i} \frac{d\Sigma_i X_i}{dt} + \frac{2}{3k_B n_b} \frac{d\mathcal{H}}{dt}, \quad (29)$$

where  $H$  is the Hubble parameter,  $k_B$  is Boltzmann's constant,  $d/dt$  is the Lagrangian derivative following each fluid element,  $n_b$  is the proper number density of all gas particles (i.e. everything except non-interacting dark matter), the symbol  $X_i$  is defined by  $n_i = (1 + \delta)X_i\rho/m_p$ ,  $n_i$  is the proper number density of species  $i$ ,  $\rho_b$  is the mean mass density of baryons,  $m_p$  is the proton mass and  $\delta$  is the mass overdensity. On the right hand side of Equation (28), the first term accounts for the adiabatic cooling driven by the Hubble expansion and is the dominant cooling term in regions with moderate and low density ( $\Delta = 1 + \delta \leq 10$ ); the second term is the adiabatic cooling/heating due to formation of the structure; the third term is for the internal energy gain or loss per particle from changing the total particle density; and the last term represents the net heat gain or loss per unit volume from radiation processes. We assume that the dominant heating mechanism is photoheating, which is a reasonable assumption for low density regions with typical temperature of  $\sim 20\,000$  K during the reionization (Efstathiou 1992; Katz et al. 1996). Other cooling mechanisms, such as adiabatic cooling and recombination cooling, can be neglected. The reason is that the adiabatic

cooling timescale of the IGM (typically  $10^9$  yr) is relatively long compared with the lifetime of QSOs (typically a few times  $10^7$  yr to  $10^8$  yr). Therefore, the adiabatic cooling can be neglected when considering the expansion of active bubbles associated with QSOs. However, the cooling mechanism can be important after the active bubbles become fossil bubbles because of the quench of their central QSOs. In our calculations, the adiabatic cooling is the dominant cooling mechanism for those fossil bubbles. Equation (29) has been solved by Hui & Gnedin (1997), which results in an asymptotic evolution in temperature of the highly ionized IGM as  $T \propto (1+z)^{0.53}$ . Therefore we simply use this asymptotic value as the temperature evolution of the IGM after reionization is complete.

The photoionization rate is given by

$$\Gamma_i = \int_{\nu_i}^{\infty} 4\pi J_\nu \sigma_i \frac{d\nu}{h\nu}, \quad (30)$$

where  $J_\nu$  is the specific intensity of the ionizing radiation as a function of frequency  $\nu$ ,  $\nu_i$  is the He II ionization threshold frequency and  $\sigma_i$  is the cross section of He II. Then the photoheating rate due to He II reionization is

$$\mathcal{H}_i = \int_{\nu_i}^{\infty} 4\pi J_\nu \sigma_i (h\nu - h\nu_i) \frac{d\nu}{h\nu}. \quad (31)$$

With the photoheating rate and the photoionization rate given above, we can obtain the expected energy injected into the IGM per ionization as

$$\langle E \rangle_{\text{He II}} = \frac{\mathcal{H}_i}{\Gamma_i} = \frac{\int_{\nu_i}^{\infty} 4\pi J_\nu \sigma_i (h\nu - h\nu_i) \frac{d\nu}{h\nu}}{\int_{\nu_i}^{\infty} 4\pi J_\nu \sigma_i \frac{d\nu}{h\nu}}. \quad (32)$$

Equation (31) implies that the increase in IGM temperature is larger if the ionizing sources have harder spectra. Ignoring the collisional ionization of He II, the corresponding increase in IGM temperature in an He III bubble, allowing for the injected energy to be shared by all the species present, is

$$k_B \Delta T = \frac{2Y_{\text{He}}}{3(8 - 5Y_{\text{He}})} \langle E \rangle_{\text{He II}} = \frac{2}{3} \frac{\langle E \rangle_{\text{He II}}}{27}, \quad (33)$$

where  $\Delta T$  is the increase in temperature,  $k_B$  is the Boltzmann constant,  $Y_{\text{He}} = 0.24$  is the primordial helium mass fraction and 27 is the number of particles over which this energy is distributed by assuming  $Y_{\text{He}} = 0.24$  (see also Abel & Haehnelt 1999).

In our model, the IGM is divided into three components: (1) the active bubbles, (2) the fossil bubbles and (3) the He II regions. As a bubble turned on, it became active until the photoionization in the bubble was balanced by the recombination. Since the relevant cooling timescale for the low density, photoionized gas in the IGM is always longer than the time that the QSO is active ( $\sim 10^8$  yr), the increase in temperature in the active bubble should stay constant (under the assumption that the heating mechanism is photoheating). In the He II regions, since there is no He II reionization taking place, the average temperature follows the thermal asymptote,  $T_{\text{He II}} \propto T_0(1+z)^{0.53}$ , in which the temperature is set by the shape of the UV background (Hui & Haiman 2003) and  $T_0$  is the IGM temperature constrained by observations at  $z \sim 6$  (Bolton et al. 2012).

Before the reionization is complete, the mean IGM temperature at the mean density is

$$T_{\text{IGM}}(z) = T_1(z) + T_2(z) + T_{\text{He II}}(z)[1 - Q_{\text{He III}}(z)], \quad (34)$$

where  $Q_{\text{He III}}(z)$  is the volume averaged fraction of ionized regions given by Equation (24), and  $T_1(z)$  and  $T_2(z)$  are the contribution from active bubbles and fossil bubbles, respectively.

Adopting an optically thin approximation (the mean energy will be weighted by the ionization cross section  $\sigma_\nu \propto \nu^{-3}$ ) and assuming an ionizing spectrum of  $J_\nu \propto \nu^{-\alpha}$ , Equation (31) reduces to  $\langle E \rangle_{\text{thin}} = 54.4(\alpha + 2)^{-1}$  eV (Abel & Haehnelt 1999). A QSO like spectrum with  $\alpha = 1.57$

gives an increase in temperature of  $\Delta T_{\text{thin}} = 4400$  K in the active bubbles. Adopting an optically thick approximation, however, all photons emitted by the source are absorbed (i.e.  $\sigma_{\text{He II}} = 1$ ) and  $\langle E \rangle_{\text{thick}} = 54.4(\alpha - 1)^{-1}$  eV, which would give an increase in temperature of about 30 000 K. Becker et al. (2011) recently reported an increase in temperature at the mean density from  $\sim 8000$  K at  $z \sim 4.4$  to  $\geq 12000$  K at  $z \sim 2.7$ . Since bubbles that ionized earlier have longer time to cool, at later times the mean increase in temperature of the IGM should be lower than that in active bubbles. Apparently, the increase in temperature in the optically thin approximation is less than that obtained by observations, but in the optically thick approximation the increase in temperature is much larger.

To reconcile the difference shown above, we set a cut-off in energy of  $E_{\text{max}} = h\nu_{\text{max}} = 350$  eV to be that obtained by numerical simulations (McQuinn et al. 2009), in which the IGM is optically thin to photons with energy above the cut-off and optically thick to photons with energy below the cut-off. With the definition of  $E_{\text{max}}$ , the corresponding increase in temperature in active bubbles is  $\Delta T_{\text{active}} = 12\,400$  K. We will adopt this value as the increase in temperature in the active bubbles. Then the volume averaged temperature contributed by the active bubble is

$$T_1(z) = \int d \log C_B \int dL_{\text{bol}} \int dM_{\bullet, f} \int_{\infty}^z dz_i \int_{z_i}^z dz' \left[ \Delta T_{\text{active}} + T_{\text{He II}}(z') \right] \\ \times \frac{dV_{\text{real}}}{dz'} \left( z'; \frac{L_{\text{bol}}}{C_B}, M_{\bullet, f}, z_i \right) \dot{G}(M_{\bullet, f}; z_i) \delta \left( L_B - \frac{\mathcal{L}_{\text{bol}}(z'; M_{\bullet, f}, z_i)}{C_B} \right) \\ \times P(\log C_B | \langle \log C_B \rangle) \Theta_1(z_{\text{eq}} - z_i), \quad (35)$$

where  $z_{\text{eq}} = z_{\text{eq}}(z, z_i)$  is the redshift at which a QSO, triggered at  $z_{\text{eq}}$ , reaches its maximum volume at  $z$ , and the step function  $\Theta_1 = 1$  for  $z_i \leq z_{\text{eq}}$  or  $\Theta_1 = 0$  for  $z_i \geq z_{\text{eq}}$ . The corresponding equilibrium timescale,  $\tau_{\text{eq}}$ , can be set by integrating Equation (18) over time until the maximum volume is reached. When the recombination in the bubbles became important, these active bubbles turned into fossil bubbles, in which temperature decreased either as  $T_{\text{fossil}} \propto (1+z)^2$  due to the adiabatic cooling or as  $T_{\text{fossil}} \propto (1+z)^{0.53}$  once a UV background was established. These temperature evolutions approximate the maximum and minimum cooling rate toward lower redshift. In fossil bubbles, we assume that once a region recombines, the temperature in this region approaches the temperature of He II regions,  $T_{\text{rec}} \sim T_{\text{He II}}$ . The reason is that at the mean density, the cooling timescale is less than the recombination timescale (Bolton et al. 2009). Then the volume averaged temperature contributed by the fossil bubble is

$$T_2(z) = \int d \log C_B \int dL_{\text{bol}} \int dM_{\bullet, f} \int_{\infty}^z \left( \frac{1+z}{1+z_{\text{eq}}} \right)^{\alpha} dz_i \int_{z_i}^z dz' \left[ \Delta T_{\text{active}} + T_{\text{He II}}(z') \right] \\ \times \frac{dV_{\text{real}}}{dz'} \left( z'; \frac{L_{\text{bol}}}{C_B}, M_{\bullet, f}, z_i \right) \dot{G}(M_{\bullet, f}; z_i) \delta \left( L_B - \frac{\mathcal{L}_{\text{bol}}(z'; M_{\bullet, f}, z_i)}{C_B} \right) \\ \times P(\log C_B | \langle \log C_B \rangle) \Theta_2(z_i - z_{\text{eq}}), \quad (36)$$

where  $\alpha = 2$  or  $0.53$  for adiabatic cooling or asymptotic cooling respectively and the step function  $\Theta_2 = 1$  for  $z_i \geq z_{\text{eq}}$  or  $\Theta_2 = 0$  for  $z_i \leq z_{\text{eq}}$ .

After the reionization is complete, the mean temperature of the IGM increases significantly and exceeds the temperature set by the UV background spectra (i.e. the asymptotic value). This biased temperature would gradually approach the asymptotic value. In the case that the temperature of the fossil bubble evolves as  $(1+z)^2$ , we simply assume that only adiabatic cooling is present once He II is fully reionized. Then the mean temperature of the IGM after the reionization would evolve as  $T_{\text{IGM}} = T_{\text{peak}}(1+z)^2$ , where  $T_{\text{peak}}$  is the peak temperature of the IGM when He II reionization is complete. This assumption, however, leads to underestimates of the temperature evolution at lower redshift, since other heating mechanisms could exist to prevent the temperature from dropping dramatically. Considering of the adiabatic heating and cooling, photoionization heating, etc.,

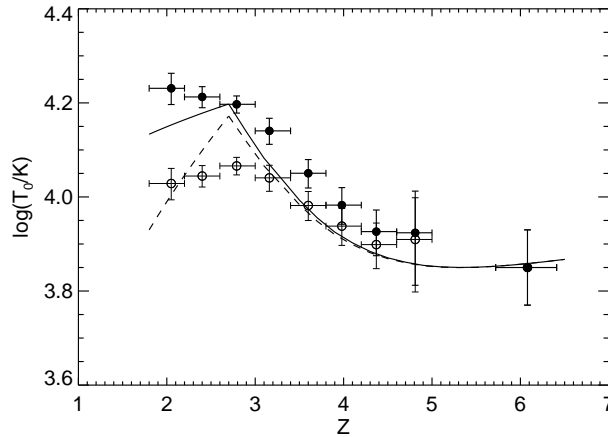


**Fig. 8** Temperature evolution of the IGM over the redshift range from  $z = 2$  to  $z = 6$ . The dashed line assumes that only adiabatic cooling is present in the fossil bubbles, while the solid line considers the thermal asymptote in these fossil bubbles. The circles represent the temperature measurements from the general Ly $\alpha$  forest at  $z \leq 5$  obtained by Becker et al. (2011) with  $2\sigma$  uncertainties. The solid and open circles represent the IGM temperature obtained by assuming an IGM temperature-density relation,  $T \propto (1 + \delta)^{\gamma-1}$ , with  $\gamma = 1.3$  and  $\gamma = 1.5$ , respectively.

the IGM temperature evolution may achieve an asymptote of  $(1 + z)^{0.53}$  as suggested by Hui & Gnedin (2003). Therefore, we also check the case of a thermal asymptote of  $T_{\text{IGM}} \propto (1 + z)^{0.53}$  if the temperature of the fossil bubble evolves as  $(1 + z)^{0.53}$ , which flattens the slope of temperature. We take  $T_{\text{IGM}} \propto (1 + z)^2$  and  $T_{\text{IGM}} \propto (1 + z)^{0.53}$  as the maximum and minimum cooling rates in the IGM respectively, and the actual temperature evolution should be between these two slopes.

Figure 8 shows a comparison between our results and the observational estimates of the IGM temperature evolution. As seen from Figure 8, our model predicts that the IGM temperature peaks at  $z \sim 2.7$ , which is consistent with the redshift of the He II reionization being completed, as shown in Figure 6 (for  $C = 3$ ). This agrees well with the measurements of the IGM temperature by Becker et al. (2011), in which they conclude that the temperature peak at  $z \sim 2.8$  indicates the reionization of He II is complete. In general, our model results are consistent with the general trend shown by observations.

Our model yields an IGM temperature evolution that follows the general trend in evolution shown by observations, though the resulting temperature from He II reionization is slightly lower. This discrepancy may come from the uncertain thermal history of the IGM, i.e., the Jeans smoothing. The small-scale structure of the Ly $\alpha$  forest depends on the thermal broadening of the absorption features, the Hubble broadening and the turbulent broadening. Heating the gas not only increases the thermal broadening but also the characteristic physical size of absorbers. Hence, a greater Hubble broadening across individual absorbers results in an additional smoothing of the Ly $\alpha$  forest. As a result, the small scale structure of the Ly $\alpha$  forest depends not only on the instantaneous temperature of the gas but also on its integrated thermal history (Pawlik et al. 2009; Becker et al. 2011). Considering the Jeans smoothing, the IGM temperature estimated from the Lyman  $\alpha$  forest (as that shown in Fig. 8) should move downward by  $\sim 2000$  K and  $\sim 1200$  K at redshifts  $z \sim 2.0 - 4.8$  and  $z \sim 6$ , respectively (Bolton et al. 2012). After considering the correction due to the Jeans smoothing, our result is quite consistent with the observations that are shown in Figure 9. There seems to only be a slight difference, if any, between the temperature evolution predicted by the model in this

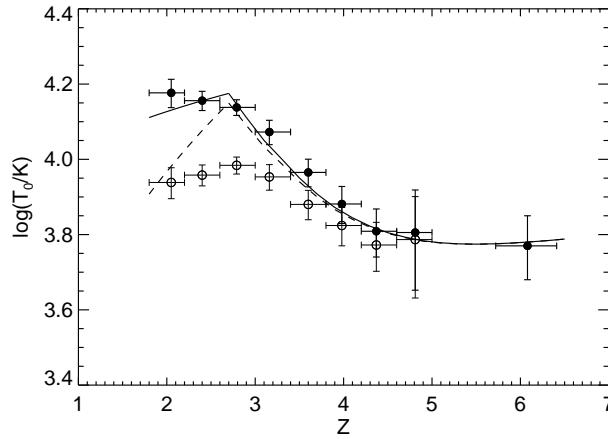


**Fig. 9** Same as Fig. 8, except also including the effect of Jeans smoothing.

paper and that obtained from observations, which could also be due to the limited number of QSOs adopted. Becker et al. (2011) and Bolton et al. (2012) only use 61 high-resolution QSO spectra over  $2.0 \leq z \leq 4.8$  and seven QSO spectra at  $z \sim 6$  to estimate the temperature evolution, which may induce some uncertainties.

## 5 DISCUSSION

The observational results obtained by Becker et al. (2011) show two trends in the temperature evolution, which are due to uncertainty in the shape of the temperature density relation, i.e.,  $\gamma$ . A flatter temperature density relation may lead to a greater increase in the IGM temperature at the mean. Becker et al. (2011) use two different slopes,  $\gamma \sim 1.5$  and  $\gamma \sim 1.3$ , which show the apparent difference at low redshift. Schaye et al. (2000) adopt an even flatter temperature density relation with  $\gamma \sim 1$  (i.e. the isothermal case), which further increases the temperature of the IGM at the mean density. So, the key point is to establish the shape of the temperature density relation and its evolution with redshift. This will clarify the evolution of  $T_0(z)$  at  $z < 4$  and allows us to determine the end of He II reionization based on the redshift at which  $T_0$  peaks (Becker et al. 2011).

In our model, there may also exist some uncertainties in the temperature evolution because of the lack of accurate treatment of the radiative transfer process. We obtain an increase in temperature of  $T = 4400$  K in the active bubbles by using the optically thin approximation and a higher increase in temperature of 12 400 K in these active bubbles by setting an energy cut-off of  $E_{\text{max}} = 350$  eV. Setting an energy cut-off in the QSO spectrum is obviously a simplification of the full radiative transfer problem (Bolton et al. 2009). During the reionization, the radiative transfer effects can largely increase the temperature in the bubbles. Since photons with higher energy have a photoionization cross section that is smaller than  $\sigma_\nu \propto \nu^{-3}$  and correspondingly larger mean free paths, the average excess energy in Equation (31) is larger at a greater distance (Abel & Haehnelt 1999; Bolton et al. 2004). Therefore, the IGM can harden and filter the ionizing radiation, imparting a significant increase in temperature in the bubbles. A detailed radiative transfer process is needed to constrain the increase in temperature in the active bubbles. The slope of the ionizing spectrum  $\alpha$  would also affect the energy that is input to the photoheating process in active bubbles (for our model, the QSO spectral index is set to  $1.57 \pm 0.17$ ). A flatter (harder) spectrum will cause a larger (smaller) energy to be input. A QSO spectrum, being unclear at high redshift, may contribute further uncertainties to the increase in temperature in these active bubbles.

## 6 CONCLUSIONS

In this paper, we construct a simple QSO model to investigate the ionization evolution and the related thermal evolution of the IGM during the reionization of He II. In our model, we simply assume that major mergers of dark matter halos are responsible for triggering QSOs, and the luminosity evolution of individual QSOs is described by the light curve in an initial accretion stage with a constant Eddington ratio and then a power-law decay driven by long term disk evolution or fueling. Once a QSO is triggered, it immediately ionizes its surrounding area as an ionized bubble. The luminosity evolution of the central QSO determines the size and volume evolution of the bubbles. As more and more bubbles emerge, they eventually overlap each other and finally permeate the whole universe. During the He II reionization, the temperature of the IGM increases due to photoheating by the ionization processes. Applying the bubble model and considering various heating and cooling mechanisms, we trace the mean thermal evolution of the IGM and obtain the average temperature of the IGM as a function of redshift. Our results are very consistent with observations. The increase in IGM temperature due to He II reionization may be determined more accurately in the future, which could put further constraints on the QSO model and the physics of He II reionization.

**Acknowledgements** This work was supported in part by the National Natural Science Foundation of China (Grant Nos. 10973017 and 11033001).

## References

- Abel, T., & Haehnelt, M. G. 1999, *ApJ*, 520, L13  
Aird, J., Nandra, K., Laird, E. S., et al. 2010, *MNRAS*, 401, 2531  
Bandara, K., Crampton, D., & Simard, L. 2009, *ApJ*, 704, 1135  
Becker, G. D., Bolton, J. S., Haehnelt, M. G., & Sargent, W. L. W. 2011, *MNRAS*, 410, 1096  
Bolton, J., Meiksin, A., & White, M. 2004, *MNRAS*, 348, L43  
Bolton, J. S., Becker, G. D., Raskutti, S., et al. 2012, *MNRAS*, 419, 2880  
Bolton, J. S., & Haehnelt, M. G. 2007, *MNRAS*, 382, 325  
Bolton, J. S., Oh, S. P., & Furlanetto, S. R. 2009, *MNRAS*, 395, 736  
Bongiorno, A., Zamorani, G., Gavignaud, I., et al. 2007, *A&A*, 472, 443  
Booth, C. M., & Schaye, J. 2010, *MNRAS*, 405, L1  
Brown, M. J. I., & Brown 2010, in *IAU Symposium*, 262, eds. G. R. Bruzual, & S. Charlot, 244  
Dijkstra, M., Haiman, Z., & Loeb, A. 2004, *ApJ*, 613, 646  
Duffy, A. R., Schaye, J., Kay, S. T., & Dalla Vecchia, C. 2008, *MNRAS*, 390, L64  
Dunkley, J., Komatsu, E., Nolta, M. R., et al. 2009, *ApJS*, 180, 306  
Efstathiou, G. 1992, *MNRAS*, 256, 43P  
Fakhouri, O., & Ma, C.-P. 2008, *MNRAS*, 386, 577  
Fakhouri, O., Ma, C.-P., & Boylan-Kolchin, M. 2010, *MNRAS*, 406, 2267  
Fan, X., Strauss, M. A., Becker, R. H., et al. 2006, *AJ*, 132, 117  
Fechner, C., Reimers, D., Kriss, G. A., et al. 2006, *A&A*, 455, 91  
Ferrarese, L. 2002, *ApJ*, 578, 90  
Furlanetto, S. R., & Oh, S. P. 2008, *ApJ*, 681, 1  
Gebhardt, K., Bender, R., Bower, G., et al. 2000, *ApJ*, 539, L13  
Giroux, M. L., & Shapiro, P. R. 1996, *ApJS*, 102, 191  
Haardt, F., & Madau, P. 2012, *ApJ*, 746, 125  
Hopkins, P. F., Richards, G. T., & Hernquist, L. 2007, *ApJ*, 654, 731  
Hui, L., & Gnedin, N. Y. 1997, *MNRAS*, 292, 27  
Hui, L., & Haiman, Z. 2003, *ApJ*, 596, 9  
Jakobsen, P., Boksenberg, A., Deharveng, J. M., et al. 1994, *Nature*, 370, 35

- Jiang, L., Fan, X., Annis, J., et al. 2008, *AJ*, 135, 1057
- Katz, N., Weinberg, D. H., & Hernquist, L. 1996, *ApJS*, 105, 19
- Larson, D., Dunkley, J., Hinshaw, G., et al. 2011, *ApJS*, 192, 16
- Madau, P., Haardt, F., & Rees, M. J. 1999, *ApJ*, 514, 648
- McGreer, I. D., Jiang, L., Fan, X., et al. 2013, *ApJ*, 768, 105
- McQuinn, M., Lidz, A., Zaldarriaga, M., et al. 2009, *ApJ*, 694, 842
- Miralda-Escudé, J., & Rees, M. J. 1994, *MNRAS*, 266, 343
- Pawlik, A. H., Schaye, J., & van Scherpenzeel, E. 2009, *MNRAS*, 394, 1812
- Richards, G. T., Strauss, M. A., Fan, X., et al. 2006, *AJ*, 131, 2766
- Schaye, J., Theuns, T., Rauch, M., Efstathiou, G., & Sargent, W. L. W. 2000, *MNRAS*, 318, 817
- Sheth, R. K., & Tormen, G. 1999, *MNRAS*, 308, 119
- Small, T. A., & Blandford, R. D. 1992, *MNRAS*, 259, 725
- Sokasian, A., Abel, T., & Hernquist, L. 2002, *MNRAS*, 332, 601
- Telfer, R. C., Zheng, W., Kriss, G. A., & Davidsen, A. F. 2002, *ApJ*, 565, 773
- Tremaine, S., Gebhardt, K., Bender, R., et al. 2002, *ApJ*, 574, 740
- Yu, Q., & Lu, Y. 2004, *ApJ*, 602, 603
- Yu, Q., & Lu, Y. 2008, *ApJ*, 689, 732
- Yu, Q., & Tremaine, S. 2002, *MNRAS*, 335, 965
- Zaroubi, S. 2013, in *Astrophysics and Space Science Library*, 396, eds. T. Wiklind, B. Mobasher, & V. Bromm, 45
- Zheng, W., Kriss, G. A., Deharveng, J.-M., et al. 2004, *ApJ*, 605, 631